

# Hydraulic Fracture Monitoring: A Jonah Field Case Study

T. Seher\*, S. Rondenay\*, and H. Djikpesse†

## ABSTRACT

Hydraulic fracturing involves the injection of a fluid to fracture oil and gas reservoirs, and thus increase their permeability. The process creates numerous microseismic events, which can be used to monitor subsurface operations. In this study we introduce a novel microearthquake relocation workflow based on cross-well seismic observations and in-situ velocity measurements, and then apply it to data from two hydraulic fracture stages conducted at the Jonah field (Wyoming). The relocation is carried out by global optimization of a probability density function including P- and S-wave traveltimes, as well as source-receiver azimuths. By averaging multiple cross-well observations, we reorient the three component receivers and reduce the scatter of measured azimuth values by 50-60%. By simultaneously relocating the observed microearthquake ensemble for one fracture stage, we derive a more reliable image of the average fracture orientation and reduce the scatter of microearthquake locations by 20-40% as compared to conventional approaches. For the two stages of fracturing investigated, the microearthquakes are found to follow a NW-SE trend that places constraints on the local stress field and on the newly created fluid paths.

(Hanson et al., 2004). The Lance formation, of late Cretaceous age, contains fluvial sandstones intercalated with overbank siltstones and mudstones (DuBois et al., 2004). The trap at Jonah is described as structural-stratigraphic. Gas entrapment is enabled by two bounding faults (Hanson et al., 2004) and a top seal (DuBois et al., 2004; Johnson et al., 2004).

The reservoir's poor connectivity and complex structure pose a challenge for the gas-recovery process, and for this reason the reservoir was not exploited commercially for many years (DuBois et al., 2004). This challenge has been overcome in recent years thanks to the development of modern completion technologies that enhance the gas recovery in tight reservoirs and have thus made the exploitation of the Jonah field viable. One such completion technique, hydraulic fracturing of the rock matrix, is commonly used to enhance production from oil and gas fields (Phillips et al., 1998). During hydraulic fracturing, fluid and proppants are injected into the reservoir to increase the connectivity of the pore space, and thereby the permeability of the host rocks. During one fracture stage in the Jonah field, 300,000 l of fluid and 68,000 kg of sand are typically injected into the reservoir at a pressure of 41 MPa (House and Shemeta, 2008).

Fluid injection and pore-pressure perturbation can modify the effective normal stress and lead to the triggering of microearthquakes (MEQ) (Shapiro et al., 1997, 1999). These MEQs can thus be used to monitor hydraulic fracturing. In particular, the location of MEQs induced by hydraulic fracturing can be used to characterize the activation of fracture systems (Maxwell et al., 2010; Li et al., 2011), to constrain fluid displacement in the subsurface (House, 1987; Phillips et al., 1998; Rutledge and Phillips, 2003; Maxwell et al., 2004), and to determine how the reservoir rocks are responding to production activity (Eisner et al., 2009).

Given the high cost of completion techniques in reservoir engineering and the possible environmental impacts of hydraulic fracturing, the monitoring of subsurface op-

## INTRODUCTION

The Jonah field in the Rocky Mountain region of Wyoming is one of the largest natural gas discoveries in the onshore United States (Robinson and Shanley, 2004). The principal reservoir rocks of the Jonah field are productive lenticular fluvial sandstones from the Lance Formation

\*Earth Resources Laboratory, Massachusetts Institute of Technology, 77 Massachusetts Ave., Cambridge, MA 02139-4307

†Schlumberger-Doll Research, One Hampshire Street, Cambridge, MA 02139-1578

erations is extremely important. MEQ observations allow monitoring of the stimulation procedure and fluid propagation in the subsurface, but interpreting MEQ observations is challenging due to location uncertainties. The main challenge stems from the fact that all receivers are typically located within a single receiver well and different observables (P- & S-wave traveltimes and P-wave azimuths) with different uncertainties are used for MEQ location.

In this paper, we conduct a systematic study of the different causes for MEQ location uncertainty to improve the precision of standard MEQ relocation procedures. The standard procedures relocate all MEQs individually. By simultaneously relocating all MEQ observations for one fracture stage, we derive a more reliable image of the subsurface distribution of seismicity. The integration of the MEQ data with coincident active source data allows us to improve the sensor orientation, which reduces the MEQ scatter. However, the active source data cannot be used to refine the velocity model.

The rest of the article is organized as follows. First, we will describe the Jonah field experiment and our data processing approach. In particular, we will demonstrate how multiple perforation shots can be used to improve the azimuth measurements for MEQ observations. Next, we develop a novel method to reduce the MEQ scatter and derive an average fracture orientation from an ensemble of MEQ measurements. Lastly, we relocate the MEQs linked to hydraulic fracturing for two fracture stages in the Jonah field.

## JONAH FIELD EXPERIMENT

Microseismic monitoring of hydraulic fracturing usually involves two or more boreholes. First, perforation shots (i.e., active, explosive sources) break the wall of the first borehole, the treatment well. This well is subsequently used to hydraulically fracture the surrounding rock through the injection of pressurized fluids, giving rise to multiple MEQs. The second borehole, the monitoring well, houses the seismic receiver array, which registers both the perforation shots and the MEQs. Normal reservoir operations are interrupted during hydraulic fracturing.

The Jonah Field experiment was a test study to develop new seismic techniques for hydraulic fracture monitoring carried out between July and September 2004. The experiment combined a time lapse vertical seismic profile experiment and a microseismic monitoring study. While the time lapse vertical seismic profile experiment gave images of the subsurface reflectivity before and after hydraulic fracturing, the microseismic study observed the subsurface changes in real time. Here, we focus on the second part of the experiment.

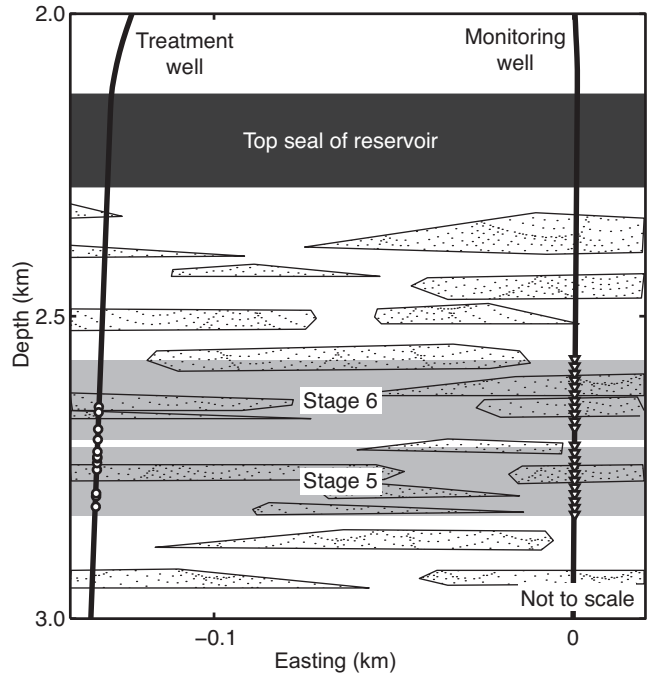


Figure 1: Sketch showing the experiment geometry. The white circles mark the perforation shots that are used to break the wall of the treatment well prior to fluid injection. The white triangles mark the locations of the receivers, that measure the seismic arrivals linked to both perforation shots and MEQs.

## Acquisition geometry and setting

In this study we analyze active and passive seismic data from two separate hydraulic fracture stages using one treatment and one monitoring well (figure 1). During each fracture stage, the treatment well was subjected to six perforation shots and the second borehole housed a seismic receiver array, which consisted of eleven three-component receivers deployed with an 11-12 m receiver spacing. The two boreholes were  $\sim 140$  m apart and the center of the receiver array was located at approximately the same depth as the explosive sources (figure 1). The seismic receivers were sampled every 0.25 ms (4 kHz) and the recordlength was 0.5 s. A single record ideally contains the seismic waves caused by a single perforation shot or MEQ. The usable frequency bandwidth of the perforation shot data is  $\sim 0.1$ -1 kHz.

## Data Processing

For single receiver wells, a standard MEQ relocation workflow usually includes the following processing steps. (1) Waveform data corresponding to the perforation shots are extracted, and used to estimate P-wave traveltimes and azimuths (figure 2)). (2) An initial velocity model is derived from well log measurements. (3) The velocity model is updated using the perforation shot traveltimes to account for possible lateral variations. (4) The per-

foration shot data are used to orient the receivers into a North-South / East-West (NS/EW) reference frame. (5) The waveform data corresponding to MEQ events are extracted and rotated into a North-South / East-West (NS/EW) reference frame. P-wave traveltimes and azimuth, as well as S-wave traveltimes, are measured (figure 3). (6) The MEQ are relocated using both traveltime and azimuth data.

Here, we adapt this standard workflow by altering or refining three of its processing steps. In step (3), we choose not to update the well log velocity model using perforation shot traveltimes as these may suffer from significant source location and origin time uncertainties. Then, in step (4), we improve the receiver orientation by averaging azimuth measurements for multiple perforation shots. Lastly, in step (6), we refine the relocation procedure by processing all MEQs simultaneously. These three modifications to the standard workflow are described in details in the next sections.

As part of our processing, synthetic traveltimes and azimuths are computed by seismic raytracing (Zelt and Barton, 1998), for a velocity model parameterized using a 10 m grid spacing in all spatial directions. Comparison with an analytic solution shows that the uncertainty related to the forward calculation is  $<0.1$  ms. Moreover, for the well log derived velocity model, we find that the benefit of taking into account ray curvature is  $<0.1$  ms (i.e., straight ray versus ray bending). While the benefit for this study is small, we use raytracing for generality of the method.

The seismic traveltimes used in this study were picked manually by industry analysts. Quality control of the traveltime picks indicates that P-wave and S-wave data quality is consistently high (figure 4). The misfit for a constant velocity model (i.e., the standard deviation after removal of a linear trend) is  $<1$  ms. In contrast with the perforation shot data (figure 2), the MEQ data show pronounced S-wave arrivals (figure 3). The absence of strong S-wave energy for perforation shots is due to the impulsive nature of the explosive sources. On the contrary, MEQs can usually be described as double-couple sources, which explains the emitted S-wave energy.

## PRIOR INFORMATION ASSESSMENT

### Velocity model estimation

We construct an initial velocity model from a well log located 240 m south of the survey area (step 2 of the standard processing sequence; see log 1 in figure 5). Since the well log measurements are highly variable we applied a 100 m moving average filter to both the P-wave and S-wave slowness measurements.

Well logs directly within the survey area were not available. To assess the lateral variability of well log velocities we applied the same processing to a second well log (log 2 in figure 5) located 470 m south-west of the survey area and 640 m west of log 1. The difference between the smoothed velocity measurements is generally  $\leq 0.1$  km/s.

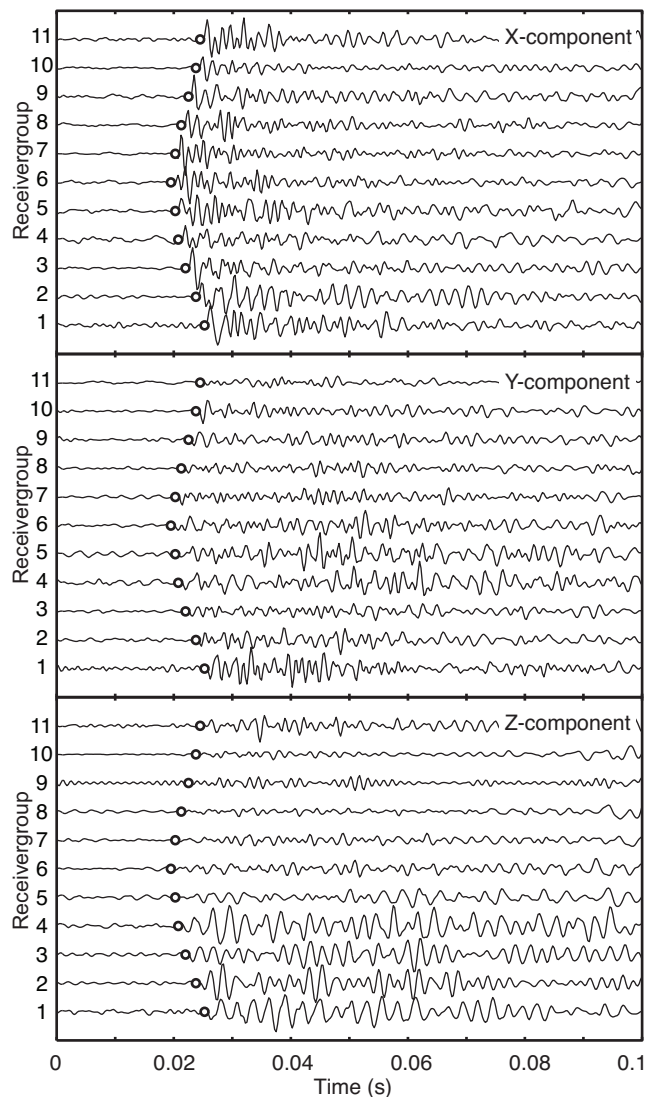


Figure 2: Seismic data for a typical perforation shot. The black circles mark the traveltime of P-waves. The seismic data were band-pass filtered between 100 Hz and 1 kHz. Single traces were normalized using pre-arrival noise energy. This assumes that the noise is homogeneous and has equal amplitude for the EW (X), NS (Y) and vertical components (Z). Next, the traces within each receiver gather were normalized to unit amplitude.

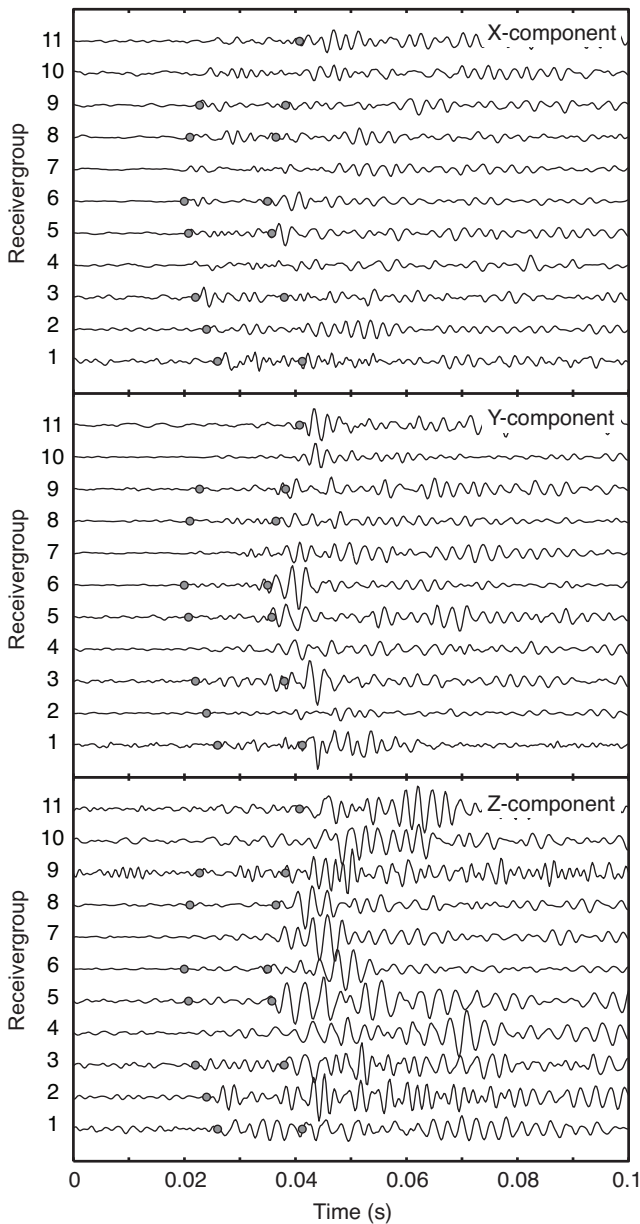


Figure 3: Seismic data for a typical MEQ. The black circles mark the traveltime of P-waves (first arrival) and S-waves (second arrival). We applied the same processing as in figure 2.

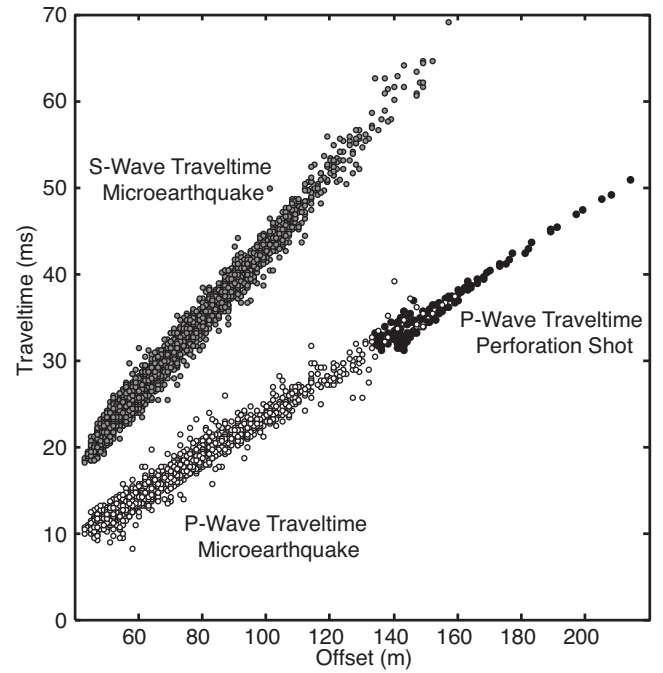


Figure 4: Comparison of traveltimes for MEQs and perforation shots for stages 5 and 6. The white and grey circles mark the P- & S-wave traveltimes for MEQs, respectively. The black circles the P-wave traveltime for perforation shots. The traveltime for the MEQs was estimated after the estimation of the origin time in the relocation process.

The small difference between the two observed well logs gives us confidence in the well log velocity model, but the uncertainty of in-situ velocities contributes to the overall traveltime uncertainty.

Recently traveltime tomography using perforation shots has been applied to calibrate the well log velocity model (Warpinski et al., 2005; Pei et al., 2009; Bardainne and Gaucher, 2010) (step 3 of the standard processing sequence). We attempted to refine the velocity model by using traveltime tomography and incorporating the well log velocities as a starting model. Traveltime tomography yielded velocities that explained the observed traveltimes, but were systematically faster than the well log velocities.

Possible causes for the mismatch between the velocity estimates and the well log velocity are a wrong source depth, a wrong origin time or a systematic bias in the velocity model. (1) A mislocation of the perforation shot may lead to a systematic misfit between observed and calculated traveltimes. (2) The origin time may be incorrect, which has a direct effect on the measured traveltimes. (3) A systematic bias in the velocity model caused by seismic anisotropy or a lateral change in velocity (the well log was recorded  $\sim 240$  m south of the survey area) may explain the difference between the predicted and observed perforation shot traveltimes.

To differentiate between these three causes for this mismatch, we estimate the seismic velocity from the per-

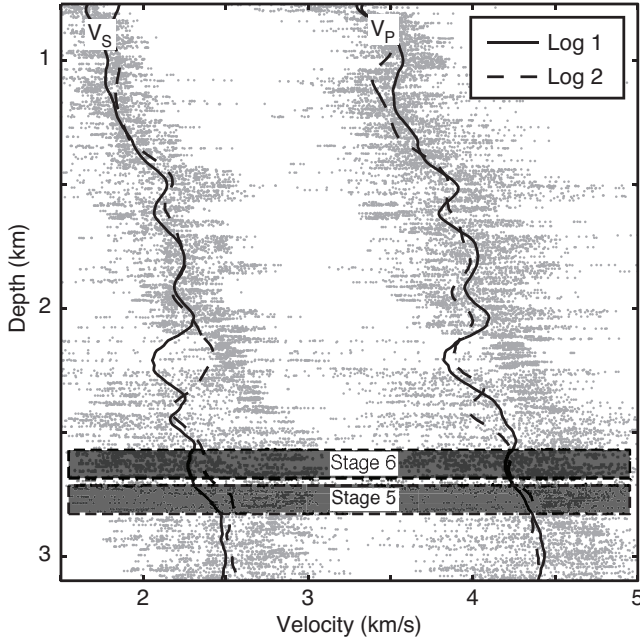


Figure 5: P-wave and S-wave velocity profiles based on well logs. The grey points and solid black line give the velocities for log 1 located  $\sim 200$  m south of the receiver well. For comparison the dashed line gives the average velocities for log 2 located in the South-West of the study area. The measured slowness values were smoothed using a 100 m moving average filter. The grey boxes mark the depth of the two fracture stages analyzed in this study.

formation shot traveltimes using two complementary approaches. (1) We derive average velocities by dividing the observed traveltimes by the source-receiver distance. A mean velocity and uncertainty can be derived by averaging the velocity measurements on different receivers for all perforation shots triggered during one fracture stage. This method requires knowledge of the origin time and source depth. (2) We derive a velocity and uncertainty estimate from the traveltime-distance gradient using linear regression and averaged the velocity measurements for all perforation shots triggered during one fracture stage. This method only requires knowledge of the source depth but not the origin time.

We apply these two methods to a total of 95 perforation shots, which were triggered during 25 fracture stages in 5 different treatment wells and observed using the same receiver well. All treatment wells were located less than  $\sim 300$  m from the monitoring well. While velocity estimates using the first method yielded velocities, that are faster than the well log measurements, velocity estimates using the second method gave velocities that are slower than the well log measurements (figure 6(a)). Since both methods used the same receiver and shot location, this discrepancy indicates a problem with the origin time.

We use the well log velocity information to calibrate the shot location and origin time. This allows us to test whether the perforation shot traveltimes are consistent

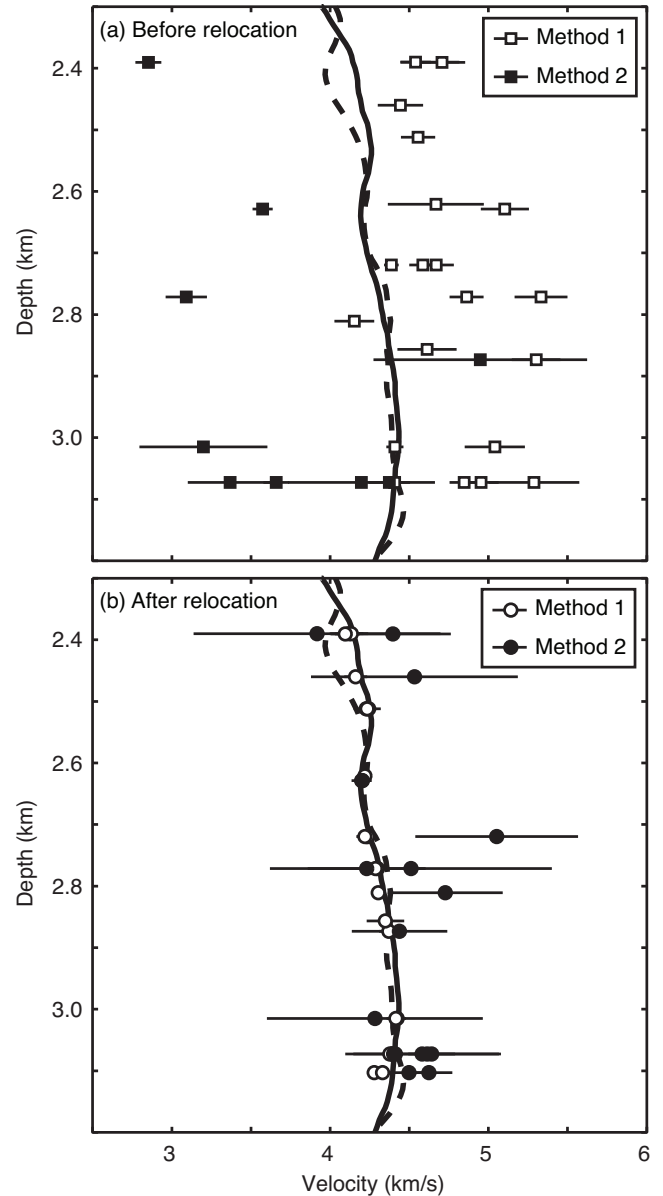


Figure 6: Comparison of smoothed well log velocities (figure 5) and perforation shot based velocity estimates before and after relocation of the perforation shots. Method 1 estimates the velocity using the traveltime and distance between the perforation shot and the receiver. Method 2 estimates the velocity using the local traveltime gradient. We only show velocity estimates with an uncertainty smaller than 10%.

with the well log assuming a reasonable error of the shot depth and origin time. We estimate synthetic traveltimes for all possible source locations within the treatment wells by tracing seismic rays through the smoothed velocity model. Since the well trajectories are known from well deviation surveys (Bulant et al., 2007), the only unknown is the shot depth; the horizontal position depends on the receiver depth. By comparing the calculated traveltimes with the measured traveltimes, we then select the source location and origin time that best fits the traveltimes observations.

Calibrating the perforation shot depth and origin time can resolve the discrepancy between the two methods (figure 6(b)). Shifting the shot depth by 22 m on average and correcting the origin time by 7 ms on average, brings the two methods in reasonable agreement with the well log velocities. The two fracture stage chosen for further analysis in this study require a depth shift of  $\sim 10$  m and a origin time correction of  $\sim 7$  ms.

In conclusion, we choose to use the well log derived velocity model in our further analysis to avoid problems related to the calibration of the velocity model. The observed traveltimes can be explained by the well log velocities to within the experiment uncertainties, which include the origin time and the source depth. Therefore, perforation shot tomography is not feasible for this experiment, because the traveltime variations are smaller than the experiment uncertainties.

## Polarization calibration

To extract useful information from the azimuth measurements, the receivers need to be oriented in a known reference frame. If the source and receiver location as well as the velocity structure are known, the orientation of the receivers can be recovered from measurements of the polarization of an incoming seismic wave (step 4 of the standard processing sequence). In this study, we assume the vertical component to be aligned with the vertical borehole axis and use perforation shots to reorient the two horizontal receiver components.

To reorient the receivers, we first calculate the true source-receiver azimuth from the known borehole geometry ( $\sim 344^\circ$ ). Next, we apply a zero-phase band-pass filter between 100 Hz and 1 kHz to the perforation shot data to increase the signal-to-noise ratio and measure the azimuth of the incoming seismic wave in a 1.5 ms time window after the traveltime pick, which encompasses the first wiggle of the seismic wave. The azimuth is determined by iteratively rotating the seismic data around the vertical axis and selecting the rotation angle that maximizes the energy on the first horizontal component (see appendix for more details). To obtain a more reliable measurement we average azimuth measurements for six perforation shots.

This approach allows us to rotate the receivers into NS/EW reference frame and reduce the scatter of azimuth measurements (figure 7). After sensor reorientation

the measured azimuth values agree with the true values. Furthermore, the scatter of measured azimuth values decreases by 50-60%. Prior to sensor rotation the orientation of the X-component was unknown; in hindsight we realized that the X-component was pointing approximately North. After rotation the X-component points approximately East.

Using the rotation angles from step 4 of the standard processing sequence, we can rotate the MEQ observations to a known reference frame (step 5 of the standard processing sequence). We apply a zero-phase band-pass filter and estimate the azimuth. To validate the sensor rotation, we cannot use the source-receiver azimuth is unknown, because the source location is unknown. However, after sensor rotation, all receivers should measure the same azimuth. We can average the azimuth measurements and calculate the azimuth misfit for the different receivers (figure 8).

While the standard deviation of azimuth residuals is approximately equal for the perforation shots and MEQ observations, the two measurements cannot be directly compared, because the MEQ azimuths show a  $180^\circ$ -ambiguity that is caused by the radiation pattern of the MEQ source mechanism. The standard deviation was measured using azimuths between  $0^\circ$  and  $360^\circ$  for the perforation shots and azimuths between  $0^\circ$  and  $180^\circ$  for the MEQs.

Recent studies have applied a reorientation of the third sensor component to assure that the vertical component is precisely vertical (Greenhalgh et al., 2005; Armstrong, 2009). This is particularly important, if the borehole axis and/or the Z-component of the receiver are not vertical. In this study we chose not to reorient the third component. Full reorientation of the sensor requires precise knowledge of the velocity structure and shot depth to be able to correctly calculate the colatitude of the incoming wavefield. Furthermore, we found that the uncertainty of colatitude measurements is typically  $\sim 10^\circ$  larger than the azimuth uncertainty. Reorientation of the third sensor is not vital for MEQ relocation, if the borehole axis is approximately vertical.

## MICROSEISMIC EVENT LOCALIZATION METHODOLOGY

### Data and model parameters

To relocate the MEQs we use P-wave traveltimes and azimuths as well as S-wave traveltimes. The traveltime uncertainty for P- and S-waves is  $\sim 6$  ms and takes into account the pick uncertainty ( $\sim 1$  ms), the uncertainty related to the forward calculation ( $< 0.2$  ms), the location uncertainty of the receivers ( $10 \text{ m} \hat{=} 2.5 \text{ ms}$  at  $\sim 4 \text{ km/s}$ ) (Eisner et al., 2009) and the uncertainties related to the velocity model ( $\pm 0.2 \text{ km/s} \hat{=} \pm 5 \text{ ms}$ ). The total uncertainty is estimated using the square root of the sum of the individual squared uncertainties. After sensor rotation all receivers should measure the same azimuth and the azimuth uncertainty can be derived from the standard

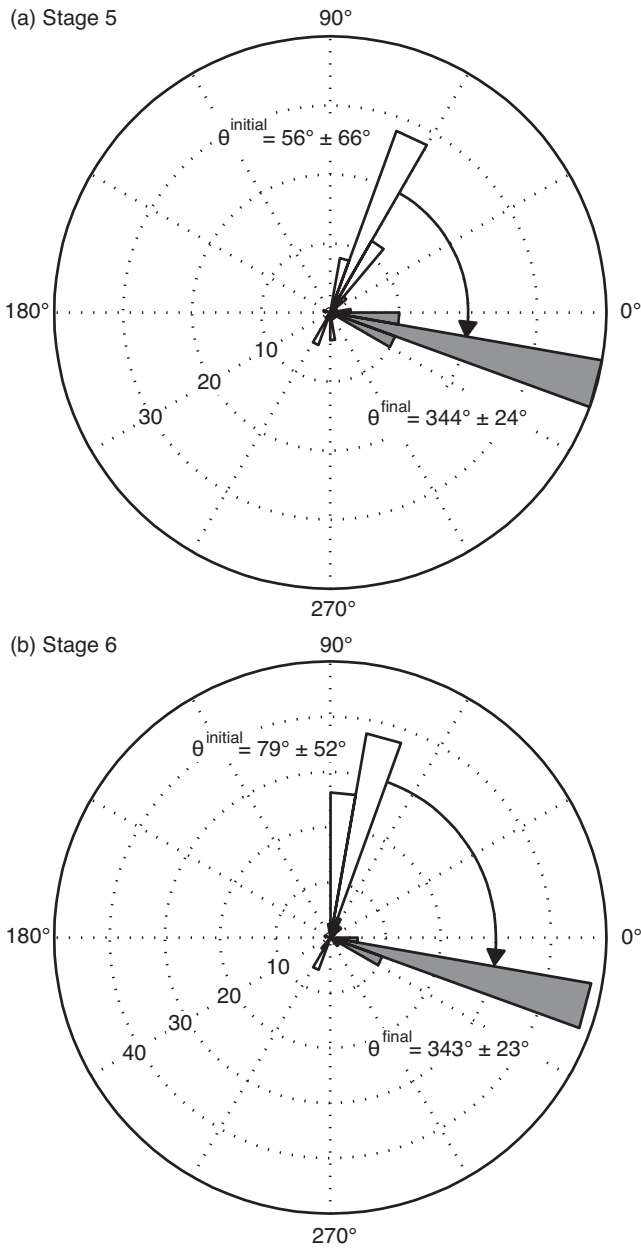


Figure 7: Statistical distribution of measured azimuth values for six shots and eleven receivers during fracture stages 5 and 6. The sensor rotation transforms the data to a NS/EW reference frame. We determine the azimuth of the incoming wavefield by maximizing the energy on one of the horizontal components. After sensor rotation the true source-receiver azimuth ( $\sim 343^\circ$ ) agrees with the measured azimuth and the scatter of measured azimuth values is reduced.

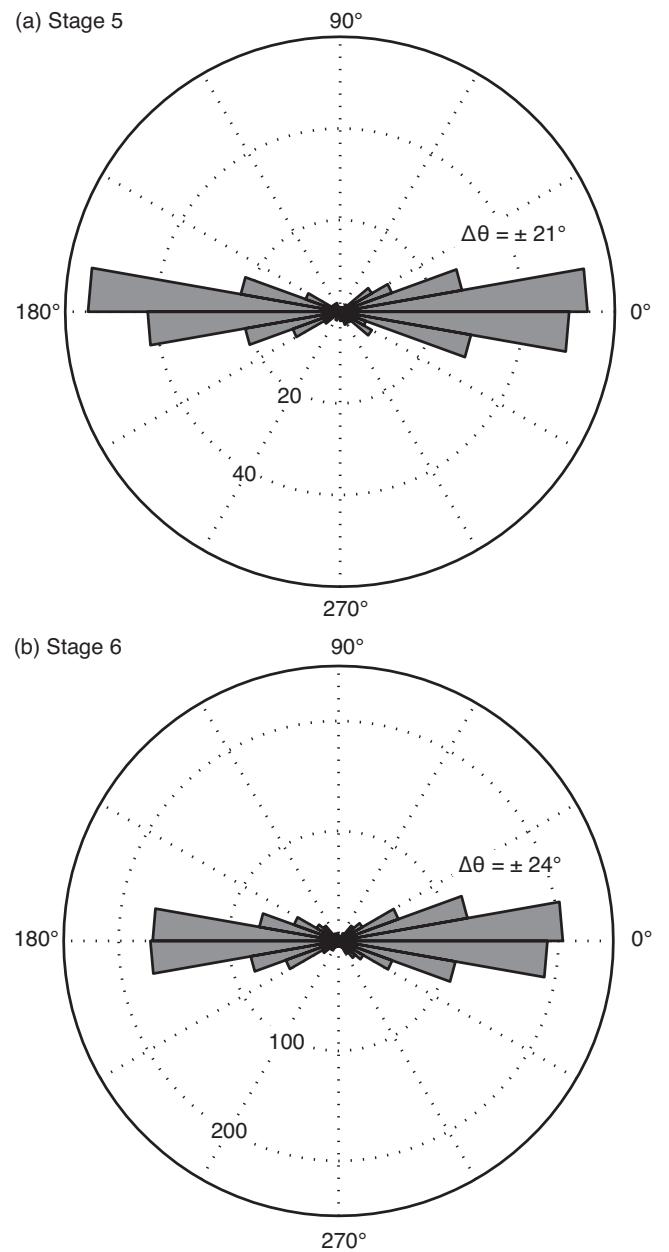


Figure 8: Difference between the measured azimuth and the average azimuth (based on all receivers for one MEQ) for all observed MEQs recorded during fracture stages 5 and 6. After relocation of the MEQs, we estimated the misfit between the calculated and measured azimuth. The  $180^\circ$ -symmetry of residuals illustrates the ambiguity in measured azimuth values, that is caused by the radiation pattern of the MEQ source.

deviation of all azimuth measurements for one MEQ. The overall azimuth uncertainty is  $\sim 20^\circ$  (figure 8).

We need to constrain four different model parameters, the origin time, the easting, the northing and the depth of the microseismic event. These model parameters are linked to the observables. If two different seismic phases have been observed, a reliable estimate of the origin time can be derived from the difference between the calculated and observed arrival times for those two different seismic phases. If the velocity structure is known, the distance to the microseismic source can be calculated from the S-P differential traveltime. The depth of the microseismic event is linked to the vertical slowness of the seismic wave. Last, the measured azimuth depends on the azimuth of the seismic event.

## Optimization problem resolution

For locating a seismic event we apply a global search technique, that determines the maximum of the probability density  $\sigma_M$  for a Gaussian model (Tarantola and Valette, 1982; Billings, 1994; Djikpéssé and Tarantola, 1999; Tarantola, 2005; Djikpesse et al., 2010)

$$\sigma_M(\mathbf{m}) \propto \exp(-S(\mathbf{m})) \quad , \quad (1)$$

where  $\mathbf{m}$  stands for the model parameter, i.e. the MEQ location. We expand the cost function  $S$  to include terms for P- and S-wave traveltimes as well as S-P differential traveltimes and azimuths:

$$\begin{aligned} S \propto & \underbrace{\sum_{i=1}^N (t_{p,i}^{calc} - t_{p,i}^{meas} - t_0)^2 / \sigma_{p,i}^2}_{\text{P-wave traveltime misfit}} \quad (2) \\ & + \underbrace{\sum_{i=1}^M (t_{s,i}^{calc} - t_{s,i}^{meas} - t_0)^2 / \sigma_{s,i}^2}_{\text{S-wave traveltime misfit}} \\ & + \underbrace{\sum_{i=1}^L (t_{s,i}^{calc} - t_{p,i}^{calc} - t_{s,i}^{meas} + t_{p,i}^{meas})^2 / (\sigma_{p,i}^2 + \sigma_{s,i}^2)}_{\text{S-P differential traveltime misfit}} \\ & + \underbrace{\sum_{i=1}^N (\theta_i^{calc} - \theta_i^{meas})^2 / \sigma_{\theta,i}^2}_{\text{Azimuth misfit}} + \lambda \underbrace{\mathcal{L}(\mathbf{m}, \mathbf{m}^{prior})}_{\text{Prior information}} \quad , \end{aligned}$$

where,  $t_p$  and  $t_s$  denote the P- and S-wave traveltimes,  $t_0$  the origin time of the MEQ and  $\theta$  the source-receiver azimuth of the seismic event.  $\sigma$  stands for the uncertainty of an observation.  $N$  and  $M$  and give the number of P- and S-wave observations and  $L$  the number of P- and S-waves that were observed on the same receiver.  $\mathcal{L}$  represents a function that links the model parameter  $\mathbf{m}$  to prior information  $m^{prior}$  about these model parameters. The parameter  $\lambda$  controls the trade-off between the data misfit and the prior information.

In this study we apply the grid search method to evaluate the cost function. We estimate traveltimes and azimuths for sources spaced 4 m apart using raytracing (Zelt and Barton, 1998). Comparing the calculated and the measured traveltimes and azimuths allows us to determine the value of the cost function in the whole model domain. The solution to the optimization problem is simply the source location that corresponds to the maximum of the probability density function.

## Prior information

The last term in the cost function allows us to introduce prior information into the relocation problem. This is a powerful way of reducing the ambiguity of the solution of the optimization problem. In particular we decided to couple the relocation problems for the different MEQs observed in this study.

To introduce knowledge about the other MEQs we applied two different types of prior information. (1) We require the MEQs to be close to the center of mass of the MEQ cloud by including a term that penalizes the distance from the center of mass. The center of the MEQ cloud is determined by averaging the locations of all MEQs during one fracture stage. The location of the treatment well is used as an initial guess for the center of the MEQ cloud. This location is then updated iteratively until the change of the average distance from the center of mass is smaller than a given threshold. This approach is similar to the collapsing method (Jones and Stewart, 1997; Fehler et al., 2000, 2001). (2) We require the MEQs to be close to a plane through the MEQ cloud. The plane runs through the center of the MEQ cloud and the plane's normal is determined by applying singular value decomposition. The smallest eigenvector is orthogonal to the fracture plane and the two largest eigenvectors lie within the fracture plane. We use the plane defined by the treatment and monitoring wells as an initial guess and then iteratively update this plane until the change of the average distance from the plane is smaller than a given threshold.

When using prior information in the solution of an optimization problem, the prior information and the data misfit need to be balanced. In this study we chose to first weight the the prior information by dividing through the distance between the treatment and monitoring well. Next, we use the parameter  $\lambda$  to scale the different parts of the cost function. To determine the parameter  $\lambda$  we first relocate the MEQs without including any prior information. This solution shows a large spread of MEQs. Next, we slowly increase  $\lambda$ , until the data misfit exceeds a threshold. Increasing  $\lambda$  increases the data misfit, but reduces the misfit with respect to the prior constraint. We selected a 5% increase of the data misfit as a threshold to terminate the search.

## RESULTS

## Event relocation

To validate our MEQ relocation procedure, we first locate a perforation shot as a ground truth test. We treat the event relocation as an unknown and test whether the recovered location agreed with the known location of the perforation shot within the borehole. Since the perforation shots used in this study do not show clear S-wave arrivals, we cannot determine the origin time based on the seismic data and we have to use the known origin time in the relocation process.

By using our relocation procedure (equation 2), we can locate the perforation shot (figure 2). The minimum of the cost function, the maximum of the probability density function, coincides with the known location of the perforation shot (figure 9(e)&(f)). P-wave traveltimes constrain the distance and to a lesser extent the depth of the seismic event (figure 9(a)&(b)). The direction of the seismic event is determined using the azimuth of the seismic event (figure 9(c)&(d)). In addition to locating the seismic source we can characterize the location uncertainty and geometry of the solution to the optimization problem (figure 9(e)&(f)). We observe that the horizontal uncertainty is smaller than the vertical uncertainty.

To illustrate our MEQ relocation procedure, we examine the different contributions to the cost function for a single MEQ (figure 3). We included P-wave and S-wave traveltimes, S-P differential traveltimes and the P-wave azimuth in the cost function (equation 2).

By using the combined P-wave and S-wave observations, we can relocate a MEQ. The S-P differential traveltimes allow us to estimate the distance and depth of the seismic event (figure 10(a)&(b)), but contain no information about the azimuth of the event. The azimuth measurement allows us again to estimate the direction to the seismic event (figure 10(c)&(d)). The contributions of P-wave and S-wave traveltimes to the cost function have the same geometry as for the perforation shot (figure 9(a)&(b)) and are not shown here. They constrain the depth and distance of the event, but not the azimuth. Finally, the cost function (figure 10(e)&(f)) shows a symmetry about the receiver array and has two distinct minima. The minimum closer to the injection point is chosen as solution to the relocation problem.

## Hydraulic fracture monitoring

The cost function defined in equation 2 allows us to introduce constraints in our relocation algorithm. In particular, it permits us to introduce information about other MEQs. This is justified, since the MEQs caused by hydraulic fracturing are not isolated events, occur in the same part of the subsurface and are caused by the same physical process.

We study the effect of two different constraints on the MEQ locations, proximity to the center of mass and prox-

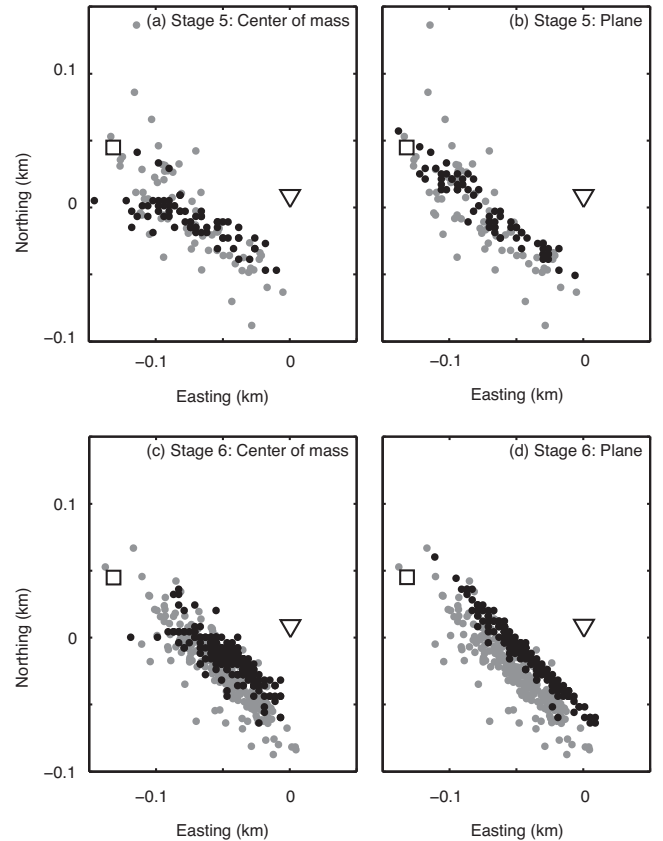


Figure 11: Comparison of MEQ relocation approaches for stages 5 (figures (a)&(b)) and 6 (figures (c)&(d)). The grey circles mark the MEQs located following the standard approach (House and Shemeta, 2008). In figures (a)&(b) the black circles mark the MEQ locations using the center of mass of the MEQ cloud as prior information. In figures (c)&(d) the black circles mark the MEQ locations using the best fitting plane through the MEQ cloud as prior information. The triangle marks the receiver location and the square the treatment well.

imity to a plane through the center of mass. To understand the effect of these constraints we compare our MEQ locations with the MEQ locations by House and Shemeta (2008).

Our MEQ locations show significantly less scattering for fracture stages 5&6. The average distance from the center of mass is reduced by  $\sim 33\text{-}34\%$  as compared to the unconstrained locations (figure 11(a)&(b)) and the average distance from the best fitting plane is reduced by 38% and 22%, respectively (figure 11(c)&(d)).

For each fracture stage the MEQs are spatially correlated and follow a NW-SE trend ( $308^\circ$  for stage 5 and  $312^\circ$  for stage 6) away from the injection well (figure 11). The best fitting planes are approximately vertical for both fracture stages (figure 12).

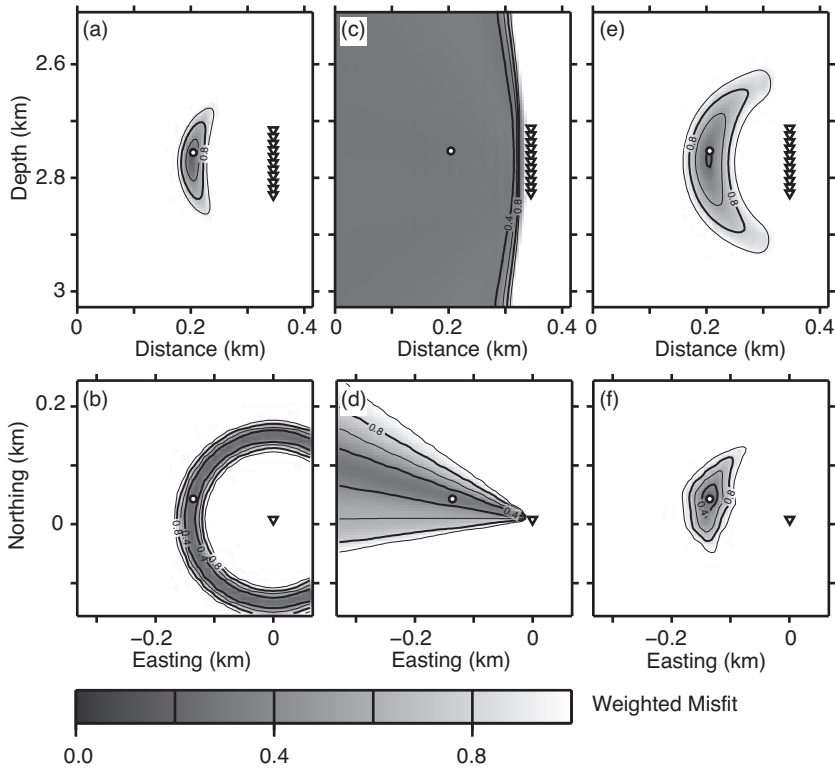


Figure 9: Relocation problem for perforation shots. The white circle marks the known location of the perforation shot and the white triangles mark the location of the receiver groups. (a)&(b) P-wave traveltimes misfit. (c)&(d) Azimuth misfit. (e)&(f) Cost function. The top rows show a vertical slice in the source-receiver plane. The bottom row show a horizontal slice at the source depth.

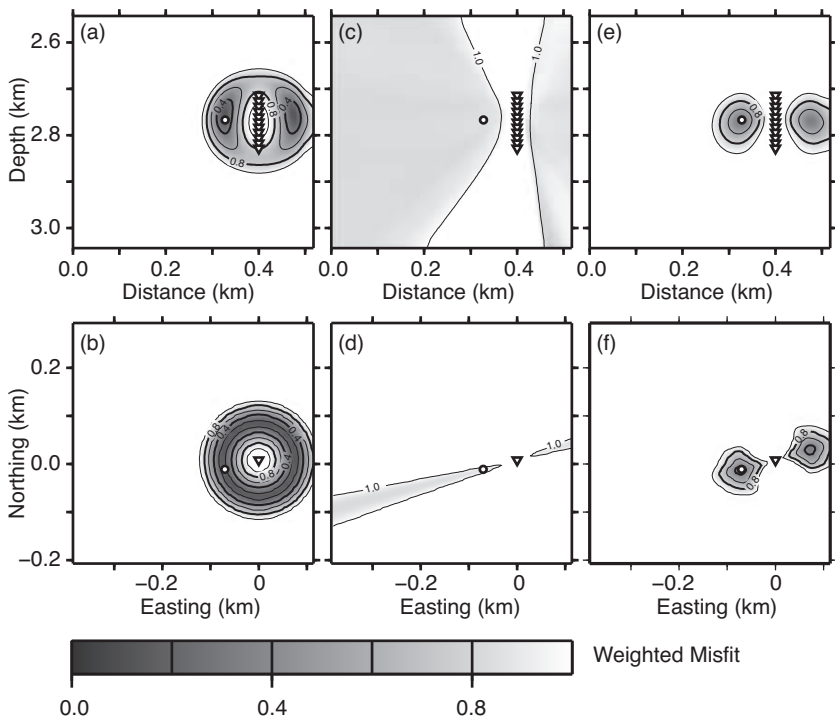


Figure 10: Location problem for MEQs. Unlike for perforation shots the origin time is unknown. However, the presence of P- and S-wave arrivals allows the estimation of the distance to the event. Combined with an estimate of the azimuth to the event, the unknown MEQ location (white circle) can be located using a single receiver well (white triangles).

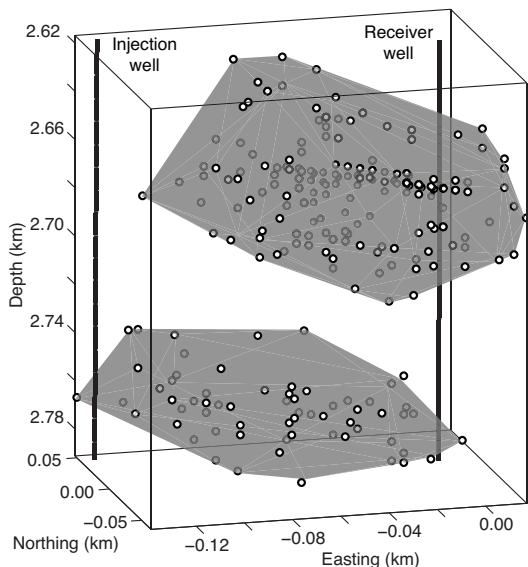


Figure 12: Three-dimensional view of all MEQs located in this study (white circles). The grey surface show the best fitting plane through the MEQ cloud.

## DISCUSSION AND CONCLUSIONS

In this paper we developed a novel MEQ relocation workflow that integrates multiple perforation shots and multiple MEQs to reduce the uncertainties of MEQ relocation. This novel workflow allowed us to reduce the scatter of MEQ locations by 20-40%, while keeping the increase in data misfit smaller than 5%.

The largest source of uncertainty in this study is the underlying velocity model, which has a significant impact on the location and spread of the MEQ cloud. To overcome the limitations of our velocity model a tomography approach seems promising. However, for this study travel-time tomography (Warpinski et al., 2005; Pei et al., 2009; Bardainne and Gaucher, 2010) using the perforation shots is not feasible, because the number of observations for each depth range is small and the traveltimes uncertainty is larger than the differential moveout between traveltimes observations. A possible approach to reduce the velocity uncertainty and improve the MEQ location would be to add additional receiver wells or surface receivers. Furthermore, one may attempt to extract the MEQ hypocenter and the velocity structure from the MEQ observations (Block et al., 1994). This seems particularly important, since changes in the velocity model due to hydraulic fracturing were ignored in this study.

The integration of active source and passive seismic data improves the MEQ relocation. The perforation shots measurements allowed us to reorient the seismic receivers. By averaging azimuth measurements for multiple perforation shots we reduced the scatter of azimuth measurements by 50-60%. These more precise az-

imuth measurements alone allowed a reduction of the spread of the MEQ cloud of 10-20%.

Our novel relocation procedure integrates information about other MEQs to better image the distribution of seismicity. The information about other nearby MEQs reduces the ambiguity inherent to the solution of the optimization problem for a single MEQ. Integrating prior constraints about the proximity to the center of mass or to a pre-defined fracture effectively reduces the spread of the MEQ cloud. In our relocation procedure, we do not assume that all observed MEQs lie on a single fracture plane. This is unlikely as the fluid penetrates the medium surrounding the treatment well. However, the existence of a dominant fracture direction is likely. Similarly, the occurrence of one earthquake influences the probability of the occurrence of the next earthquake. Integration of this information would require more rigorous analysis.

The relocation procedure developed in this study allows us to extract specific information from the data. By iteratively updating the MEQ cloud with respect to a prior constraint, we can find the most likely center of mass or dominant fracture direction of one MEQ cluster. The extension of this method to testing more complex fracture growth models seems promising. Integrating additional constraints as prior information effectively allows testing, whether certain models are consistent with the observed seismic data.

We have demonstrated that we can derive significant trends from a cloud of MEQ locations. For this study the MEQs follow approximately NW-SE trend. MEQs related to hydraulic fracturing commonly appear aligned in bands parallel to the maximum horizontal stress direction and reactivate pre-existing fractures (Willis et al., 2007). This implies that trends in the distribution of MEQ allow the characterization of the local stress field. Furthermore, the zone of seismicity is commonly associated with the zone of major fluid paths (House, 1987). Thereby, the MEQ cloud allows us to characterize the direction of newly created permeability.

## ACKNOWLEDGEMENTS

This work was made possible by funding from MIT's Earth Resources Laboratory and Schlumberger-Doll-Research. We would like to thank Julie Shemata and Nancy House for sharing their results and giving us access to their seismic data. We greatly profited from discussions with Mark Willis, Elizabeth LaBarre and Francois Auzeais.

## APPENDIX POLARIZATION ANALYSIS

Polarization analysis of the incoming wavefield is an important technique used for sensor reorientation (see MacBeth, 2002, chapter 4) and MEQ relocation. Since many different algorithm for polarization analysis exist, we compare the behavior of three simple algorithms to select one suitable to our problem. To determine the direction of the incoming seismic wave, we have explored three different approaches based on singular value decomposition of the covariance matrix for each receiver gather (CSVD), singular value decomposition of the complete three component recordings for each receiver gather (SVD) and energy maximization on one of the recorded components by rotation of the sensor using a grid search method (GS).

In the CSVD approach, we first carry out covariance analysis for every receiver gather in a time window after the picked P-wave arrival (Montalbetti and Kanasevich, 1970; Perelberg and Hornbostel, 1994). The length time window comprises the first wiggle. The components of the covariance matrix are given by  $\mathbf{P}_{ij} = \text{Cov}(\mathbf{X}_i, \mathbf{X}_j)$ , where  $\mathbf{X}_1$ ,  $\mathbf{X}_2$  and  $\mathbf{X}_3$  represent the measured seismic data on the three receiver components, respectively. Next, we apply singular value decomposition  $\mathbf{P} = \mathbf{U}\mathbf{S}\mathbf{V}^T$  to the covariance matrix. The eigenvector  $e$  corresponding to the largest eigenvalue is either parallel or anti-parallel to the propagation of motion of the incoming P-wave (Jurkevics, 1988; Greenhalgh and Mason, 1995; Greenhalgh et al., 2005). The azimuth  $\theta$  and colatitude  $\phi$  can be estimated from the components of the eigenvector  $e$  using the following trigonometric relationships  $\theta = \arctan\left(\frac{e_1}{e_2}\right)$  and  $\phi = \arccos(e_3)$ .

The SVD approach determines the directionality of the incoming P-wave using singular value decomposition of the three component recordings for each receiver  $\mathbf{X} = \mathbf{U}\mathbf{S}\mathbf{V}^T$  (de Franco and Musacchio, 2001). This very similar to the approach described above, except that we do not first apply covariance analysis. Instead the singular value decomposition is applied directly to the data in a time window after the P-wave pick. We use the same time window as for the CSVD approach.

The GS approach searches azimuth  $\theta$  and colatitude  $\phi$  of the incoming wave by maximizing the energy on one of the receiver components with respect to the other two components. We apply the time window after the first arrival as before. Using the following equations we iteratively rotate the seismic traces and retain those values of  $\theta$  and  $\phi$ , that maximize the following equation:

$$\underset{\theta \in [0, 2\pi[}{\text{argmax}} \left( \frac{\sum_{i=1}^N (\cos \theta \cdot x_{1,i} - \sin \theta \cdot x_{2,i})^2}{\sum_{i=1}^N (\sin \theta \cdot x_{1,i} + \cos \theta \cdot x_{2,i})^2} \right) \quad (3)$$

$$\underset{\phi \in [0, \pi[}{\text{argmax}} \left( \frac{\sum_{i=1}^N (\cos \phi \cdot \tilde{x}_{1,i} + \sin \phi \cdot x_{3,i})^2}{\sum_{i=1}^N (-\sin \phi \cdot \tilde{x}_{1,i} + \cos \phi \cdot x_{3,i})^2} \right) \cdot \quad (4)$$

We first maximize the energy on one of the horizontal components using equation 3. The numerator and denominator in equation 3 measure the energy in the  $\mathbf{X}_1$ - and  $\mathbf{X}_2$ -component after rotation about the angle  $\theta$ . By

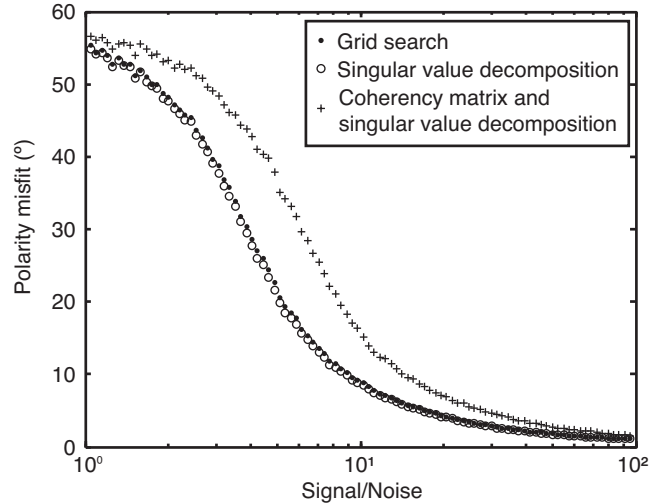


Figure 13: Comparison of different methods for the estimation of the direction of the incoming wavefield. The signal-to-noise ratio gives the ratio between the synthetic signal and noise. The average difference between the true direction and the calculated direction is estimated by averaging over all possible directions. Here, direction includes both azimuth and colatitude.

maximizing equation 3 with respect to  $\theta$  we maximize the energy on the  $\mathbf{X}_1$ -component with respect to the  $\mathbf{X}_2$ -component. The value  $\theta$  that maximizes equation 3 is the azimuth of the incoming wavefield. We rotate the horizontal traces about  $\theta$  to concentrate the seismic energy on the  $\mathbf{X}_1$ -component and then apply the same technique to the rotated  $\mathbf{X}_1$ -component and the  $\mathbf{X}_3$ -component. The value  $\phi$  that maximizes equation 4 is the colatitude of the incoming wavefield.

A comparison of the three approaches (CSVD, SVD and GS) is provided in figure 13, that shows the mean misfit between the calculated and the measured direction of a synthetic P-wave arrival. We calculated synthetic data for seismic sources distributed regularly around a receiver in a constant velocity medium. The synthetic data had a central frequency of 30 Hz and were contaminated with Gaussian noise having a signal-to-noise ratio between 1 and 100. After applying a time window of 6 ms after the P-wave arrival (the first wiggle), we measured the direction of the incoming wave. The mean misfit is obtained by averaging the misfit for all seismic events surrounding the receiver. While the three methods give similar misfits at the low and high signal-to-noise ratio (figure 13), the SVD and the GS approach yield better results for intermediate signal-to-noise ratios.

## REFERENCES

- Armstrong, P., 2009, Model-based relative bearing estimation for a downhole multicomponent sensor array: SEG Technical Program Expanded Abstracts, SEG, 4100–4104.
- Bardainne, T., and E. Gaucher, 2010, Constrained tomography of realistic velocity models in microseismic monitoring using calibration shots: *Geophys. Prosp.*, **58**, 739–753.
- Billings, S., 1994, Simulated annealing for earthquake location: *Geophys. J. Int.*, **118**, 680–692.
- Block, L. V., C. Cheng, M. C. Fehler, and W. S. Phillips, 1994, Seismic imaging using microearthquakes induced by hydraulic fracturing: *Geophysics*, **59**, 102–112.
- Bulant, P., L. Eisner, I. Pšenčík, and J. Calvez, 2007, Importance of borehole deviation surveys for monitoring of hydraulic fracturing treatments: *Geophys. Prosp.*, **55**, 891–899.
- de Franco, R., and G. Musacchio, 2001, Polarization filter with singular value decomposition: *Geophysics*, **66**, 932–938.
- Djikpesse, H., P. Armstrong, R. Rufino, and A. Hawthorn, 2010, Reducing uncertainty with seismic measurements while drilling: *IEEE Transactions on Instrumentation and Measurement*, **59**, 4–14.
- Djirkpéssé, H., and A. Tarantola, 1999, Multiparameter l1 norm waveform fitting: Interpretation of Gulf of Mexico reflection seismograms: *Geophysics*, **64**, 1023–1035.
- DuBois, D., P. Wynne, T. Smagala, J. Johnson, K. Engler, and B. McBride, 2004, Geology of Jonah field, Sublette County, Wyoming, *in* *Jonah Field: Case Study of a Giant Tight-Gas Fluvial Reservoir*: Rocky Mountain Association of Geologists, volume **52** of *AAPG Studies in Geology*, 37–59.
- Eisner, L., P. M. Duncan, W. M. Heigl, and W. R. Keller, 2009, Uncertainties in passive seismic monitoring: *Leading Edge*, **28**, 648–655.
- Fehler, M., A. Jupe, and H. Asanuma, 2001, More than cloud new techniques for characterizing reservoir structure using induced seismicity: *Leading Edge*, **20**, 324–328.
- Fehler, M., W. Phillips, L. House, R. Jones, R. Aster, and C. Rowe, 2000, Improved relative locations of clustered earthquakes using constrained multiple event location: *Bull. Seism. Soc. Am.*, **90**, 775–780.
- Greenhalgh, S., and I. Mason, 1995, Orientation of a downhole triaxial geophone: *Geophysics*, **60**, 1234.
- Greenhalgh, S., I. Mason, and B. Zhou, 2005, An analytical treatment of single station triaxial seismic direction finding: *J. Geophys. Eng.*, **2**, 8–15.
- Hanson, W., V. Vega, and D. Cox, 2004, Structural geology, seismic imaging, and genesis of the giant Jonah gas field, Wyoming, USA, *in* *Jonah Field: Case Study of a Giant Tight-Gas Fluvial Reservoir*: Rocky Mountain Association of Geologists, volume **52** of *AAPG Studies in Geology*, 61–92.
- House, L., 1987, Locating microearthquakes induced by hydraulic fracturing in crystalline rock: *Geophys. Res. Lett.*, **14**, 919–921.
- House, N., and J. Shemeta, 2008, Understanding hydraulic fractures in tight-gas sands through the integration of borehole microseismic data, three-dimensional surface seismic data, and three-dimensional vertical seismic profile data: A Jonah field case study, *in* *Understanding, exploring, and developing tight-gas sands*: AAPG, AAPG Hedberg Series, No. 3, 77–86.
- Johnson, R., T. Finn, and R. Roberts, 2004, Regional stratigraphic setting of the Maastrichtian rocks in the Central Rocky Mountain Region, *in* *Jonah Field: Case Study of a Giant Tight-Gas Fluvial Reservoir*: Rocky Mountain Association of Geologists, volume **52** of *AAPG Studies in Geology*, 21–35.
- Jones, R. H., and R. C. Stewart, 1997, A method for determining significant structures in a cloud of earthquakes: *J. Geophys. Res.*, **102**, 8245–8254.
- Jurkevics, A., 1988, Polarization analysis of three-component array data: *Bull. Seism. Soc. Am.*, **78**, 1725–1743.
- Li, J., H. Zhang, H. S. Kuleli, and M. N. Toksoz, 2011, Focal mechanism determination using high-frequency waveform matching and its application to small magnitude induced earthquakes: *Geophys. J. Int.*, **184**, 1261–1274.
- MacBeth, C., 2002, Multi-component VSP analysis for applied seismic anisotropy: Pergamon Press, **26**.
- Maxwell, S. C., J. Rutledge, R. Jones, and M. Fehler, 2010, Petroleum reservoir characterization using downhole microseismic monitoring: *Geophysics*, **75**, 75A129–75A137.
- Maxwell, S. C., T. I. Urbancic, J. H. L. Calvez, K. V. Tanner, and W. D. Grant, 2004, Passive seismic imaging of hydraulic fracture proppant placement: SEG Technical Program Expanded Abstracts, 560.
- Montalbetti, J. F., and E. R. Kanasevich, 1970, Enhancement of teleseismic body phases with a polarization filter: *Geophys. J. R. astr. Soc.*, **21**, 119–129.
- Pei, D., Q. J.A., B. Cornish, D. Quinn, and W. N.R., 2009, Velocity calibration for microseismic monitoring: A very fast simulated annealing (VFSA) approach for joint-objective optimization: *Geophysics*, **74**, WCB47–WCB55.
- Perelberg, A., and S. Hornbostel, 1994, Applications of seismic polarization analysis: *Geophysics*, **59**, 119–130.
- Phillips, W., T. Fairbanks, J. Rutledge, and D. Anderson, 1998, Induced microearthquake patterns and oil-producing fracture systems in the Austin chalk: *Tectonophysics*, **289**, 153–169.
- Robinson, J., and K. Shanley, eds., 2004, *Jonah field: Case study of a tight-gas fluvial reservoir*: Rocky Mountain Association of Geologists, volume **52** of *AAPG Studies in Geology*.
- Rutledge, J., and W. Phillips, 2003, Case history hydraulic stimulation of natural fractures as revealed by induced microearthquakes, Carthage cotton valley gas

- field, east texas: *Geophysics*, **68**, 441–452.
- Shapiro, S., E. Huenges, and G. Borm, 1997, Estimating the crust permeability from fluid-injection-induced seismic emission at the KTB site: *Geophys. J. Int.*, **131**, F15–F18.
- Shapiro, S. A., P. Audigane, and J. Royer, 1999, Large-scale in situ permeability tensor of rocks from induced microseismicity: *Geophys. J. Int.*, **137**, 207–213.
- Tarantola, A., 2005, *Inverse problem theory and methods for model parameter estimation*: Society for Industrial and Applied Mathematics.
- Tarantola, A., and B. Valette, 1982, Inverse problems = quest for information: *J. Geophys.*, **50**, 150–170.
- Warpinski, N., R. Sullivan, J. Uhl, C. Waltman, and S. Machovoe, 2005, Improved microseismic fracture mapping using perforation timing measurements for velocity calibration: *SPEJ*, **10**, 14–23. (SPE-84488-PA).
- Willis, M., D. Burns, R. Lu, M. Toksoz, and N. House, 2007, Fracture quality from integrating time-lapse VSP and microseismic data: *Leading Edge*, **26**, 1198–1202.
- Zelt, C., and P. Barton, 1998, Three-dimensional seismic refraction tomography: A comparison of two methods applied to data from the Faroe Basin: *J. Geophys. Res.*, **103**, 7187–7210.